



UNIVERSITÀ
DEGLI STUDI
FIRENZE

FLORE

Repository istituzionale dell'Università degli Studi di Firenze

CMEs from AR 10365: Morphology and Physical Parameters of the Ejections and of the Associated Current Sheet

Questa è la Versione finale referata (Post print/Accepted manuscript) della seguente pubblicazione:

Original Citation:

CMEs from AR 10365: Morphology and Physical Parameters of the Ejections and of the Associated Current Sheet / SCHETTINO G.; POLETTI G.; ROMOLI M.. - In: THE ASTROPHYSICAL JOURNAL. - ISSN 0004-637X. - STAMPA. - 708:(2010), pp. 1135-1144. [10.1088/0004-637X/708/2/1135]

Availability:

The webpage <https://hdl.handle.net/2158/383059> of the repository was last updated on

Published version:

DOI: 10.1088/0004-637X/708/2/1135

Terms of use:

Open Access

La pubblicazione è resa disponibile sotto le norme e i termini della licenza di deposito, secondo quanto stabilito dalla Policy per l'accesso aperto dell'Università degli Studi di Firenze (<https://www.sba.unifi.it/upload/policy-oa-2016-1.pdf>)

Publisher copyright claim:

La data sopra indicata si riferisce all'ultimo aggiornamento della scheda del Repository FloRe - The above-mentioned date refers to the last update of the record in the Institutional Repository FloRe

(Article begins on next page)

CMEs FROM AR 10365: MORPHOLOGY AND PHYSICAL PARAMETERS OF THE EJECTIONS AND OF THE ASSOCIATED CURRENT SHEET

G. SCHETTINO¹, G. POLETTI², AND M. ROMOLI¹

¹ Dipartimento di Astronomia e Scienza dello Spazio, Università di Firenze, Largo Enrico Fermi 2, 50125 Florence, Italy; giulia@arcetri.astro.it

² INAF-Osservatorio Astrofisico di Arcetri, Largo Enrico Fermi 5, 50125 Florence, Italy
Received 2009 August 20; accepted 2009 November 18; published 2009 December 17

ABSTRACT

We study the evolution and physical parameters of three consecutive coronal mass ejections (CMEs) that occurred at the west limb of the Sun on 2003 June 2 at 00:30, 08:54, 16:08 UT, respectively. The Large Angle and Spectrometric Coronagraph Experiment (LASCO) CME catalog shows that the CMEs entered the C2 field of view with position angles within a 5° interval. This suggests a common origin for the ejections, to be identified with the magnetic system associated with the active region that lies below the CMEs. The close proximity in time and source location of the events prompted us to analyze LASCO white light data and Ultraviolet Coronagraph Spectrometer (UVCS) spectra with the aim of identifying similarities and differences among the three CMEs. It turns out that two of them display the typical three-part structure, while no conclusion can be drawn about the morphology of the third ejection. The CMEs plasma is “cool,” i.e., electron temperatures in the CMEs front are of the order of 2×10^5 K, with no significant variation between different events. However, ejection speeds vary by a factor of ~ 1.5 between consecutive events and electron densities (more precisely emission measures) by a factor of ~ 6 between the first CME and the second and third CMEs. In the aftermath of all events, we found evidence of current sheets (CSs) both in LASCO and UVCS. We give here the CS physical parameters (electron temperature, density, and kinetic temperature) and follow, in one of the events, their temporal evolution over a 6 hr time interval. A discussion of our results, in the framework of previous findings, concludes the paper.

Key words: Sun: coronal mass ejections (CMEs) – Sun: UV radiation

Online-only material: color figures

1. INTRODUCTION

A coronal mass ejection (CME) represents a sudden and spectacular ejection of up to 10^{16} g of plasma from the Sun to the interplanetary medium with speeds that range from several tens km s^{-1} (*slow* CMEs) to a few thousand km s^{-1} (*fast* CMEs). The general consensus is that the ejection is produced by a loss of equilibrium in the magnetic configuration and that magnetic reconnection plays a fundamental role in the generation and evolution of CMEs.

CMEs often show a typical “three-part structure” (Hundhausen 1987), consisting in a bright frontal loop, a dark cavity underneath, and an embedded bright core, which has been in some case identified as an eruptive prominence seen edge-on (e.g., Chen et al. 1997). Sometimes CMEs have a more complex configuration, but the interpretation of the three-dimensional geometry usually is not trivial because of projection effects.

Many CME models have been proposed up to now. In particular, in the “catastrophe models” (e.g., the “flux rope model” by Lin & Forbes 2000) reconnection is responsible for the loss of equilibrium and leads to the formation of a current sheet (CS), which extends from the top of the reconnected loop system to the CME bubble.

Over the last decade a better knowledge of the structure and physical properties of CMEs and associated CSs has been obtained through the analysis of the spectra acquired by the *Ultraviolet Coronagraph Spectrometer* (UVCS), on board of the *Solar and Heliospheric Observatory* (SOHO). Also, sometimes it has been possible to reconstruct the CMEs geometry combining Doppler shift measures with speeds in the plane of the sky (POS; e.g., Ciaravella et al. 2006). Electron temperatures at heliocentric distances of 1.5 – $1.6 R_\odot$ in the CME

front show a wide range of values, from 6×10^3 K (Ciaravella et al. 1997) to 2×10^6 K (Bemporad et al. 2007). Electron density has also been inferred in the front structure: Bemporad et al. (2007) obtained a value of $1.0 \times 10^7 \text{ cm}^{-3}$ at $1.6 R_\odot$, while Ciaravella et al. (2005) derived densities in the range 4×10^6 – $4 \times 10^7 \text{ cm}^{-3}$ at $2.3 R_\odot$.

CSs have been detected in UVCS spectra and analyzed by, e.g., Ciaravella et al. (2002), Ko et al. (2003), Lin et al. (2005) and Bemporad et al. (2006): CSs have been identified from the emission of ions with high charge states, which are not observed in the quiet corona. Their width (i.e., size normal to the radial direction) has been inferred from the portion of UVCS slit where high temperature ion emission was observed: values obtained are, e.g., 1.3×10^5 km at $1.5 R_\odot$ (Ko et al. 2003), 6.8×10^4 km (Lin et al. 2005), and 1.4×10^5 km (Ciaravella & Raymond 2008) at $1.7 R_\odot$. Indeed, the measured width of the CS is much larger than the expected width, which is supposed to be on the order of a gyroradius. Lin et al. (2009) suggested a variety of processes that may enhance the resistivity resulting in a broadened CS whose size might match the measured width. However, recently Liu et al. (2009a) pointed out that the heliospheric current sheet has a typical size of about 200 proton gyroradii ($<10^4$ km) and it is embedded in a plasma sheet whose dimension (10^5 km) is comparable to the width of the UVCS “CS.” Hence, these authors suggest that UVCS observations should be interpreted in terms of the plasma sheet around the undetectable CS. In the following, to facilitate comparison with previous works, we will keep referring to the observed UVCS/Large Angle and Spectrometric Coronagraph Experiment (LASCO) features as “CSs,” but the reader should be aware that we are dealing, most likely, with a plasma sheet.

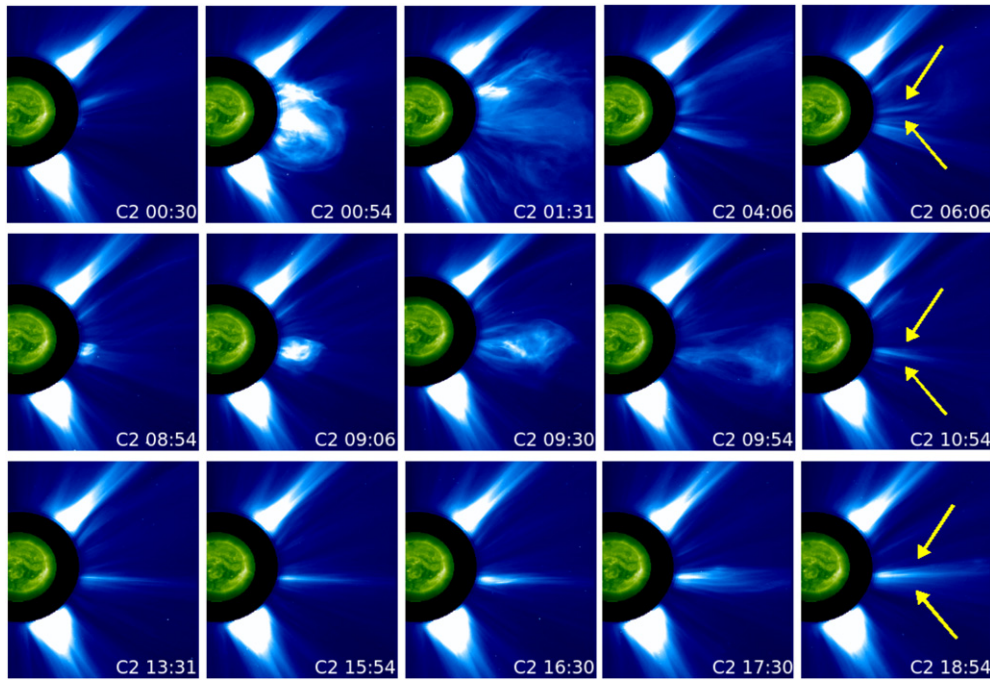


Figure 1. LASCO C2 images of the three CMEs observed on 2003 June 2. Top: the 00:30 UT event; middle: the 08:54 UT CME; bottom: the 16:06 UT event. Inside each LASCO image we show the EIT image in Fe XII–195 Å, acquired at the time closest to the corresponding LASCO image. The arrows point to structures identified as plasma sheets.

(A color version of this figure is available in the online journal.)

The physical parameters of CSs have been inferred from UVCS data. Electron temperatures T_e turn out to be on the order of $3\text{--}6 \times 10^6$ K (Ciaravella et al. 2002; Ko et al. 2003) at $1.5 R_\odot$ and slightly higher ($4\text{--}8 \times 10^6$ K; Ciaravella & Raymond 2008) at $1.7 R_\odot$. Electron densities vary from $4 \times 10^7 \text{ cm}^{-3}$ (Ko et al. 2003) at $1.5 R_\odot$ and $(3\text{--}10) \times 10^7 \text{ cm}^{-3}$ at $1.7 R_\odot$ (Ciaravella & Raymond 2008). Yet our knowledge of CSs is very limited: for instance we do not know how CS physical parameters vary with heliocentric distance and little is known about their change in time.

In this paper, we study the coronal evolution of three consecutive CMEs that apparently originate from the same source, trying to infer the differences in physical properties of the three events and of the associated CSs. The three CMEs occur at the west limb on 2003 June 2 above the same active region (AR), over a time interval of about 17 hr, and are well covered by UVCS observations.

The paper is organized as follows. After a brief description of the 2003 June 2 scenario (Section 2) and of the UVCS observations (Section 3), we study the morphology of the three events as inferred from LASCO C2 images and from UVCS spectra (Section 4) and we analyze the physical properties of the CME fronts and of the associated CSs (Section 5). A discussion of our results concludes the paper.

2. THE THREE CMEs OF 2003 JUNE 2

The LASCO CME catalog gives for the three CMEs on 2003 June 2 the onset times of, respectively, 00:30, 08:54, and 16:06 UT and position angles (P.A.s), measured counterclockwise from the north pole, P.A. = 265° , 261° , 260° . At approximately the same position we find NOAA AR 10365, which, on June 2, covered the P.A. interval $250^\circ\text{--}265^\circ$.

Representative LASCO C2 images of the events are shown in Figure 1. The first two CMEs show the typical three-part

structure, observed for many CMEs as described above. On the contrary, the third CME does not show this structure and looks like a jet; this could be due to a projection effect, as will be discussed later. LASCO CME catalog gives for the three CMEs a speed projected onto the POS of, respectively, about 1600, 1000, and 600 km s^{-1} , so they can be classified as “fast” CMEs.

We inferred the CME properties by analyzing UV spectra from the *Ultraviolet Coronagraph Spectrometer* (UVCS), as well as images from the LASCO instruments on *SOHO*. A detailed description of the morphology of the CMEs from LASCO images and from UVCS spectra, acquired at lower heliocentric distances, will be given in Section 4. In the following, we illustrate the UVCS configuration during the observations.

3. THE UVCS OBSERVATIONS

The three CMEs briefly described in the previous section have been partially covered by UVCS observations. UVCS took data from 23:46 UT on June 1 to 02:05 UT on June 2, from 06:08 UT to 15:58 UT, and from 16:01 UT to 17:30 UT on June 2. The UVCS parameters for each of the data sets are summarized in Table 1.

The strongest lines detected in the first and second observation intervals are the O VI 1031.9–1037.6 Å doublet and the H I Ly β lines in the first order and the Si XII 499.4 Å line in the second order. The data sets also include the [Fe XVIII] 974.9 Å and the C III 977.0 Å lines: the first line is usually used for the diagnostics of CSs (e.g., Ciaravella et al. 2002; Ko et al. 2003; Raymond et al. 2003; Bemporad et al. 2006), while the second, because of its very low temperature of maximum formation ($T_{\text{max}} \simeq 8 \times 10^4$ K), does not originate in the corona and is used to correct lines for straylight contamination.

The third data set is part of a synoptic observation program, where data are acquired sequentially with P.A. from 0° to 360° in

Table 1
UVCS Parameters for the Observations

| Parameters | Data Sets I and II | Data Set III |
|-------------------------------------|--|---|
| Observation time (UT) | 23:46, June 1–02:05, June 2 (set I) 06:08–15:58, June 2 (set II) | 16:01–17:30, June 2 |
| P.A. ^a (deg) | 263 | 270 |
| Heliocentric height (R_{\odot}) | 1.7 | 1.5, 1.7, 1.9, 2.1, 2.5, 3.1 |
| Slit width (μm) | 98 | 151 |
| Spatial binning (pxl) | 6 (42") | 3 (21") |
| Exposure time (minutes) | 2 | 2 |
| Spectral ranges (\AA) | 1024.0–1043.2, 1005.0–1013.1, 998.0–1002.0, 967.2–981.1, 943.4–966.3 | 1024.4–1042.7, 966.6–978.9 (1204.7–1216.1 in red. channel) |
| Spectral binning (pxl) | 2 (=0.2 \AA , I–IV spectral range); 3 (=0.3 \AA , V spectral range) | 2 (=0.2 \AA , 0.18 \AA in red. channel) |

Note.

^a Position angle of the radial through the center of the UVCS slit, measured counterclockwise from the north pole.

Table 2
Spectral Lines Detected in the UVCS Data Sets

| λ_{lab} (\AA) | Ion | Transition | $\log T_{\text{max}}$ | Data Set |
|---|------------|---|-----------------------|------------|
| 1215.67 | H I | Ly α | 4.5 | III |
| 520.66 | Si XII | $1s^2 2s^2 S_{1/2} - 1s^2 2p^2 P_{1/2}$ | 6.3 | III |
| 1037.61 | O VI | $2s^2 S_{1/2} - 2p^2 P_{1/2}$ | 5.5 | I, II, III |
| 1031.91 | O VI | $2s^2 S_{1/2} - 2p^2 P_{3/2}$ | 5.5 | I, II, III |
| 1025.72 | H I | Ly β | 4.2 | I, II |
| 499.37 | Si XII | $2s^2 S_{1/2} - 2p^2 P_{3/2}$ | 6.3 | I, II |
| 977.02 | C III | $2s^2 1S_0 - 2s 2p^1 P_1$ | 4.9 | I, II, III |
| 974.86 | [Fe XVIII] | $2p^5 2P_{3/2} - 2p^5 2P_{1/2}$ | 6.8 | I, II |
| 972.54 | H I | Ly γ | 4.3 | I, II |
| 950.15 | [Si IX] | $2p^2 3P_1 - 2p^2 1S_0$ | 6.0 | I, II |
| 944.38 | [Si VIII] | $2p^3 4S_{3/2} - 2p^3 2P_{1/2}$ | 5.9 | I, II |

45° steps at different altitudes. Here we analyzed the data taken at P.A. = 270° at the subsequent heliocentric heights of 3.1, 2.5, 2.1, 1.9, 1.7, and 1.5 R_{\odot} . The strongest lines detected in the third data set are the O VI 1031.9–1037.6 \AA and H I Ly α lines. The lines identified in each data set are listed in Table 2, with their theoretical wavelength, the ion which produces the line, its atomic transition, and the temperature of maximum formation.

All data sets have been calibrated using the standard routines of the Data Analysis Software (ver. DAS40); line intensities have been calculated by integrating over the line profile and subtracting the adjacent background. Straylight correction turned out to be relevant only for the O VI and H I Lyman lines.

4. LASCO MORPHOLOGY AND UVCS SPECTRA ANALYSIS OF THE THREE EVENTS

4.1. The First Event

The morphology of this event and its temporal evolution, as observed by the two-dimensional Doppler coronagraph *Norikura Green-Line Imaging System* (NOGIS) at the Norikura Solar Observatory, has been described by Hori et al. (2005); here we summarize their scenario and we complement it with the information derived from UVCS data. The authors identified two different magnetic systems before the eruption, one originating in the flare-productive NOAA AR 10365 (P.A. = 250°–265°) and one overlying a quiescent filament (P.A. = 290°–265°) made up of a bundle of face-on coronal loops. According to the *GOES* event list, at 23:23 UT on June 1 a C9.1 flare occurred in AR10365; then, about 1 hr before the CME, the southern end of the face-on loop system, at the interface with the AR, became

active in EUV, suggesting a link between the two magnetic flux systems, while dense, hot (2 MK) plasma sowed up above the AR. At 23:46 UT the flare emission was followed by the eruption of the filament. At 00:05 UT on June 2 NOGIS observed a blueshifted dark bubble, identified as the CME, expanding from the interface between the AR and the face-on loops system, while the Nobeyama Radioheliograph (NoRH) revealed a 17 GHz emission in AR10365 from 00:05 to 00:10 UT. At 00:07 the AR produced a M6.5 flare, detected by *GOES*, and at the same time NOGIS observed a blueshifted jet northern of the CME, ejected upward above the interface of the two neighboring magnetic flux systems. Moreover, metric type II bursts were observed around 00:20 UT.

LASCO CME catalog shows that the CME entered the LASCO C2 field of view (FOV) between 00:30 and 00:48 UT (see Figure 1, top panel) with an average POS speed of 1656 km s⁻¹ and an acceleration of 42.5 m s⁻². Also, it is possible to recognize the blueshifted jet, described by Hori et al. (2005), northern of the CME bubble.

UVCS observations started right at the time of the filament eruption. The distribution of O VI 1031.9 \AA and Si XII 499.4 \AA line intensities along the UVCS slit, over the observing interval, is shown in Figure 2, where the position along the slit (x -axis) is converted to P.A. and the y -axis gives the time of observation. The intensity maps have been obtained by subtracting from the measured value of the intensity at each pixel along the UVCS slit the average value of intensity measured at the same pixel in the pre-CME corona. The Ly β and O VI 1037.6 \AA maps are not shown here because, although noisier, they look quite similar to the O VI 1031.9 \AA map.

At 00:23 UT a blueshifted bright emission appears in O VI map, with a concave shape, over a latitude interval that includes the AR. This brightening is produced by the CME front reaching the 1.7 R_{\odot} level, where the UVCS slit is set. From LASCO CME catalog the CME reaches 2.55 R_{\odot} at 00:30 UT, hence we infer a projected speed of the CME between 1.7 and 2.55 R_{\odot} of about 1550 km s⁻¹, consistent with the speed and acceleration provided by LASCO catalog. The front structure shows an average Doppler shift of -1.0 \AA both in O VI and Ly β lines and is consistent with the result found by Hori et al. (2005), who identified the CME front with the observed blueshifted bubble.

The Si XII map (Figure 2, left panel) is noisier than the O VI map, but the pre-CME AR emission is still well visible. At 00:14 UT, just before the front appeared in O VI map, a bright Si XII area shows up, ahead of the CME front. Figure 2 shows, around

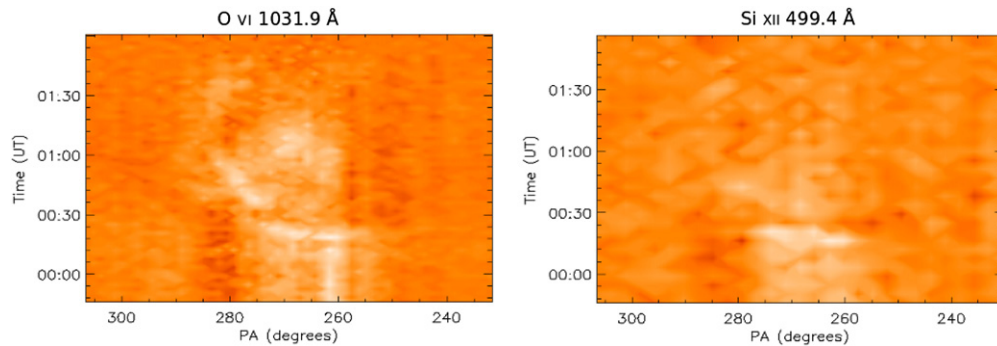


Figure 2. Left: O VI 1031.9 Å intensity evolution along the UVCS slit (P.A.s, x-axis) with time (y-axis). Right: same as top left for the Si XII 499.4 Å line. (A color version of this figure is available in the online journal.)

00:20 UT, a limited time interval over which simultaneous brightenings of O VI and Si XII seem to occur. However, the Si XII intensity enhancement cannot be ascribed to the front, because the Si XII line is unshifted, while the O VI and Ly β lines are blueshifted in the front. The lack of emission in hot lines in the front, although not common, has been observed in other events (e.g., Ciaravella et al. 1997, 1999, 2003). The brightening in Si XII takes place simultaneously with the radio type II bursts, which, as discussed by Wild (1950), Nelson & Melrose (1985), and Mancuso et al. (2002), are usually believed to be generated by the magnetohydrodynamic shock ahead of the CME. It has been a long matter of debate whether metric type II bursts are produced by CME-driven shocks or flare blast waves (e.g., Cliver et al. 1999; Vrřnak & Cliver 2008); only recently unambiguous evidence for the origin of a metric type II burst from a CME-driven shock has been provided by high cadence observations from *STEREO*/SECCHI (Liu et al. 2009b). Hence, the bright area in Si XII may be generated by shock-excited plasma in front of the CME.

We also look for further spectroscopic signatures of the shock passage. In particular in previous works (Raymond et al. 2000; Mancuso et al. 2002; Raouafi et al. 2004; Ciaravella et al. 2005), the most relevant shock associated features observed by UVCS were a dimming and a sudden broadening of the O VI lines profile, together with the brightening of spectral lines from high order ions. The first effort can be ascribed to Doppler Dimming in the high outflow speed plasma after the passage of the shock; while heating of the shocked plasma, or else non-thermal effects, can account for the line broadening. However, in the UVCS spectra there is no significant change in the O VI 1031.9 Å line intensity/width at the time of the shock passage. Hence, it is not clear whether the enhanced Si XII emission is due to the presence of a shock: an alternative interpretation in terms of plasmoids is illustrated in Schettino et al. (2009).

After the passage of the CME, three bright ray-like structures show up in LASCO white light images at P.A. = 278°, 249°, and 239°, respectively. The first and the third structures are visible for about 1 hr after the CME ejection and are detectable in the UVCS spectra in [Fe XVIII] 974.9 Å line from 01:00 UT to the end of the first set of observation (02:05 UT). Because these angles correspond, respectively, to the north edge of the blueshifted jet and the south edge of the CME bubble, these hot structures originate from the lateral compression of the ambient coronal plasma by the CME expanding plasma. The central feature (P.A. = 249°), instead, appears in LASCO C2 images after the others, at 02:30 UT, and lasts until the passage of the second CME. This ray-like structure aligned with the [Fe XVIII] UVCS emission motivated its identification with the

CS produced after a CME predicted by the Lin & Forbes (2000) model, but apparently forms after the end of the UVCS observations (02:05 UT) as we could not find any signature of this structure in the first UVCS data set. However, UVCS [Fe XVIII] emission at this latitude is observed from the very beginning of the second set of UVCS observations (06:08 UT), leading us to interpret it as emission from the CS of the earlier CME, which apparently forms about 2 hr after the CME ejection. Hence, we conclude that UVCS data bear evidence of the CME front and of a (delayed) CS, associated with this event. We cannot say whether a delayed formation of a CS is a common or uncommon feature in CME associated CSs, because (see Section 6), as of today, only two data sets have been analyzed which cover the time of CME ejection (in both of them the CS formed shortly after the CME ejection), while all other studies examine observations which started some time after the event.

4.2. The Second Event

As shown in Figure 1 (middle panel), the second CME takes place a few degrees below the first CME, right above the AR10365, which we identify as the source of the CME. At the time of the CME ejection, the Learmonth Observatory observed an eruptive prominence at the west limb at P.A. = 259° from 08:33 to 08:53 UT and an associated M3.9 flare at 08:41 UT.

As for the first CME, we looked for evidence of the passage of the CME through the UVCS slit: an intensity enhancement, which can be ascribed to the CME front crossing the UVCS slit, has been detected in O VI 1031.9–1037.6 Å, in H I Ly β and C III lines.

Figure 3 shows the intensity maps of the O VI 1031.9 Å and C III 977.0 Å lines, obtained as described for the first CME. From these maps we infer that the CME front crosses the UVCS slit at 08:39 UT. This allows us to derive a POS speed from the UVCS slit altitude to the base of the LASCO C2 FOV of 1080 km s⁻¹ with an uncertainty of 10%, in good agreement with the POS speed of 980 km s⁻¹ given by the CME LASCO catalog. Opposite to the case studied in Section 4.1, this front looks inhomogeneous. We have also studied the O VI 1031.9 Å Doppler shift throughout the data set (see Figure 4). It turns out that the CME front is blueshifted and the blueshift decreases in time until no shift is detected after 09:00 UT. The front has a mean blueshift of -0.6 Å, which corresponds to an average line-of-sight (LOS) speed of 170 km s⁻¹. From the ratio between the LOS and the POS speed inferred above we conclude that the CME either propagates slightly toward us (blueshifted) or expands asymmetrically. Whatever the cause, the shift decreases in time until no shift is detected. After the passage of the

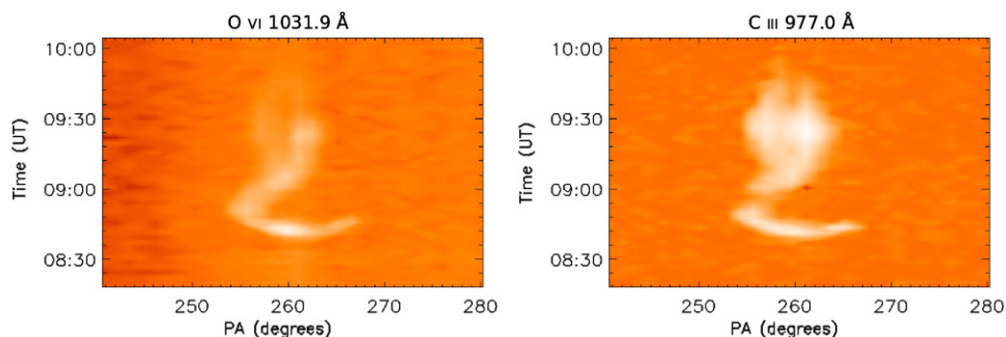


Figure 3. O VI 1031.9 Å (left) and C III 977.0 Å (right) intensity maps for the 08:54 UT CME.

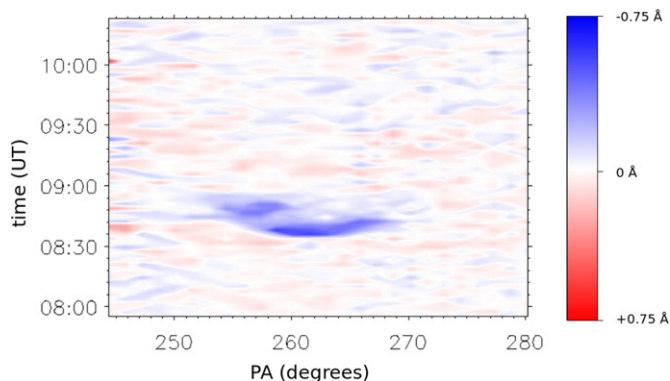


Figure 4. O VI 1031.9 Å Doppler shift contour map for the 08:54 UT CME.

front, a cool “stem” shows up, possibly branching off in two structures, at a position where, according to the Lin & Forbes (2000) predictions, we might expect a hot CS.

Indeed UVCS spectra show evidence of this structure in both [Fe XVIII] 974.9 Å and Si XII 499.4 Å lines from 09:40 UT to the end of data set (15:58 UT). Also, the LASCO C2 images show the formation of a ray-like structure after the passage of the CME, which lasts until the onset of the third CME. The evolution in time of the CS is shown in Figure 5, which gives the LASCO C2 difference images at different times. The position of the UVCS slit is also shown. We point out that the CS has a fragmented structure and slowly shifts in time to lower latitudes. We conclude that this structure is the CS formed after the second CME. The CS lies some degrees northern of the CS formed after the first CME. We did not find any evidence in UVCS data of the earlier CS after the passage of the second CME. The [Fe XVIII] line intensity distribution along the UVCS slit versus

time is shown in Figure 6: intensities have been summed over 20 minutes time intervals to obtain a better statistics. The [Fe XVIII] line intensity is enhanced over the interval $253^\circ \leq \text{P.A.} \leq 266^\circ$ and isocontours show position and time intervals where the [Fe XVIII] intensity is higher by 3σ than the mean value along the slit at that time. We refer the reader to the Schettino et al. (2009) paper, where a detailed study of the front and the CS of this event are presented.

4.3. The Third Event

The third CME occurs at about the same P.A. (P.A. = 260°) as the second CME, just above AR10365. An eruptive prominence at limb at P.A. = 259° , associated with a flare at 15:38 UT, has also been observed by Holloman Observatory from 15:38 UT to 16:23 UT. According to the LASCO CME catalog, this CME reaches a heliocentric distance of $3.0 R_\odot$ at 16:06 UT, with a POS speed of 645 km s^{-1} . This is consistent with the bright feature observed at the same P.A. by UVCS in O VI 1031.9–1037.6 Å and in H I Ly α lines from the very beginning of the third data set (16:01 UT), at $3.1 R_\odot$.

We already pointed out that LASCO images of this CME do not show evidence of the typical three-part structure, observed in the first two events. The jet-like appearance of this CME may be due to a projection effect if the three-part structure lies in a plane perpendicular to the POS. To infer the CME structure we made an analysis of the Doppler shift of UVCS spectral lines, but we could not reach any conclusive result. The O VI and Ly α lines are not shifted at $3.1 R_\odot$, while are slowly blueshifted, at the lower heliocentric heights sampled later on, up to a maximum shift of -0.4 Å . On the contrary, the C III 977.0 Å line, which is a relatively faint line, visible in our data only at $1.9 R_\odot$ and $1.7 R_\odot$, shows both a blueshifted and a redshifted component at adjacent pixels along the slit, thus suggesting that the observed structure

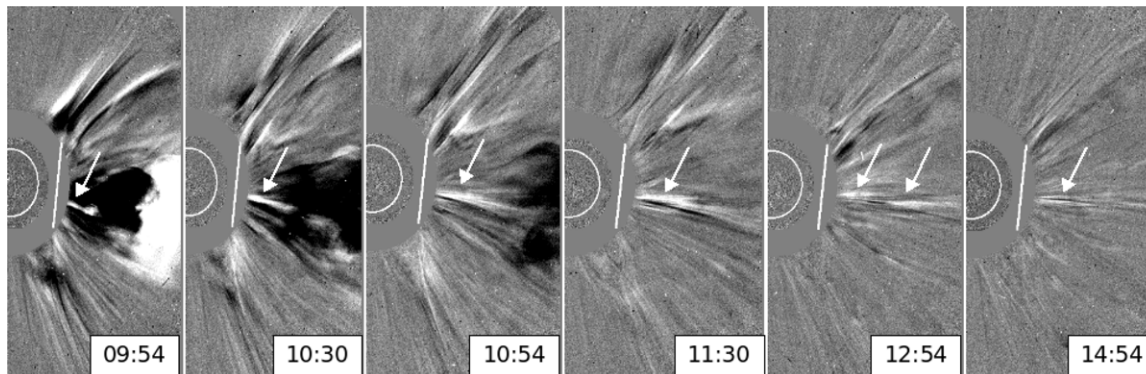


Figure 5. LASCO C2 difference images for the evolution of the CS after the second CME. The arrows show evidences of a plasma sheet.

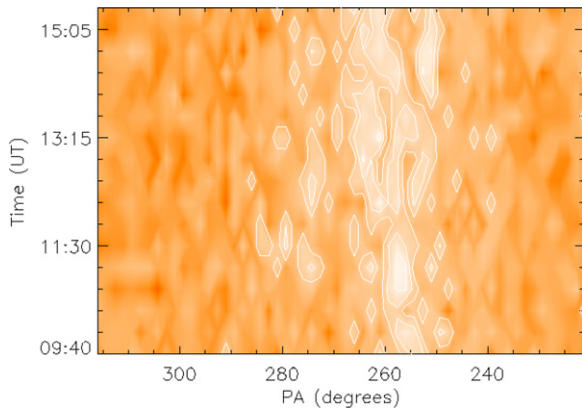


Figure 6. [Fe xviii] line intensity distribution along the UVCS slit obtained as in Figure 3. Isocontours give position and time intervals where the [Fe xviii] line intensity is higher by 3σ than the mean value along the slit at that time. (A color version of this figure is available in the online journal.)

and the LOS lie on the same plane. At later times and lower altitudes ($1.5 R_{\odot}$) the C III line is not visible, probably because the CME emission is fading. Hence lines give controversial indications and we cannot say whether we are looking at a structure lying in a plane normal to the POS or to a complex helical structure. The way data have been acquired, with higher altitudes sampled first, prevents us from describing the evolution in time of the CME, as no individual structure can be followed in time.

As for the first two CMEs, also after the third CME a bright ray-like feature appears in LASCO white light images, from about 19:30 UT, and seems to slowly fade throughout the next day. Unfortunately, the UVCS slit, at that time, was moved in its synoptic scan to other P.A.s and we have no means to support the white light CS identification with UVCS data. We note that no signature of the second CME CS is recognizable in LASCO images after the third CME ejection.

5. PHYSICAL PARAMETERS OF THE THREE CMEs

In the following, we give the physical parameters of the front and of the CS of the two earlier events. We also derived temperature and emission measure in the third CME ejection, but, because of its peculiar configuration, we are unable to identify the structure they refer to.

5.1. Physical Parameters of the Front

5.1.1. The Front of the First CME

As we can see from Figure 2, the CME front clearly shows up in the O VI 1031.9 Å line and can be identified also in the O VI 1037.6 Å and H I Lyβ 1025.7 Å lines.

In the solar corona, O VI and H I lines form by radiative and collisional excitation. In the presence of plasma motions the radiative component may completely vanish because of Doppler dimming (Hyder & Lites 1970): in this case the value of the intensity ratio R of the 1031.9 to the 1037.6 Å O VI doublet lines is 2, as if the lines form by collisional excitation only. However, pumping effects may contribute to rebuild the radiative line component, provided the excited radiation is Doppler shifted by the correct amount (Noci et al. 1987). In the CME front it turns out that the intensity ratio of 1031.9–1037.6 Å O VI lines is around 2: this means that at the speed of the CME the pumping of O VI 1037.6 Å by O VI 1031.9 Å and of O VI 1031.9 Å by H I Lyβ (Raymond & Ciaravella 2004) is not yet significant and the

O VI 1031.9 Å and H I Lyβ lines are only collisionally formed. The intensity of a collisionally excited line is

$$I_{\text{coll}}(X_a) \simeq \frac{1}{4\pi} A_X C_{X_a}(T_e) \text{EM} \text{ (photons cm}^{-2} \text{ s}^{-1} \text{ sr}^{-1}), \quad (1)$$

where X_a is a generic ion of the element X , A_X is the abundance of the element X with respect to hydrogen, $G(T) = A_X C(T)$ is the contribution function, proportional to the collisional excitation coefficient and to the ionization balance of the ion, evaluated at the temperature of the maximum formation of the ion, and EM is the emission measure, defined as $\text{EM} = \int_{\text{LOS}} N_e^2 dl$, where N_e is the electron density and the integration is computed along the LOS.

Equation (1) shows that it is possible to give an estimate of the electron temperature T_e from the ratio of line intensities using the relation:

$$\frac{I(X_a)}{I(Y_a)} = \frac{A_X C_{X_a}(T_e)}{A_Y C_{Y_a}(T_e)}, \quad (2)$$

where X_a and Y_a are two generic ions of the elements X and Y , whose abundance is known. Using the coronal abundance ratio $\frac{A_O}{A_H} = 7.8 \times 10^{-4}$ (Feldman et al. 1992), the $C(T_e)$ curves derived by CHIANTI database (ver. 5.2), with the ionization balances from Mazzotta et al. (1998), and the intensity of O VI 1031.9 Å and Lyβ measured in the front, we derived a temperature $T_e = 1.6 \times 10^5$ K.

Once the electron temperature is known, we can use Equation (1) to derive the value of the emission measure EM. From the O VI 1031.9 Å measured intensity we inferred a value $\text{EM} = (8 \pm 1) \times 10^{24} \text{ cm}^{-5}$.

5.1.2. The Front of the Second CME

The transit of the second CME through the UVCS slit is revealed by an intensity enhancement of O VI 1031.9–1037.6 Å, H I Lyβ 1025.7 Å, and C III 977.0 Å lines in UVCS spectra (see Figure 3), while the Si XII 499 Å line intensity does not show any variation with respect to the quiet corona emission. Also in this event we find that the intensity ratio of the O VI doublet lines in the CME front is about 2 and we assume that the O VI 1031.9 Å line formed only by collisional excitation. Because in these conditions the C III line as well forms only by collisional excitation (Corti et al. 2007), we inferred a value of electron temperature $T_e = 1.6 \times 10^5$ K, from the ratio of O VI 1031.9 Å to C III line intensities, with $\frac{A_O}{A_C} = 2.0$ (Feldman et al. 1992) and the ionization balances from Mazzotta et al. (1998). We chose to use the C III line instead of the Lyβ line (the only line besides the O VI doublet observed in the first CME front), because it is statistically more significant. However, from the ratio of O VI 1031.9 Å to Lyβ we found a value of electron temperature consistent with the one derived using C III line. We conclude that the electron temperature in the front of the first two CMEs is the same.

From Equation (1) and the measured O VI 1031.9 Å line intensity we derived an emission measure $\text{EM} = (5 \pm 1) \times 10^{25} \text{ cm}^{-5}$, 6 times larger than in the earlier event.

5.1.3. The Third CME

As noted above, the interpretation of the morphology of this eruptive event is not obvious. At each heliocentric height we found one or more peaks in the emission profile along the UVCS slit of O VI doublet lines and H I Lyα lines. The peaks show, depending on the time of observation, no Doppler shift or

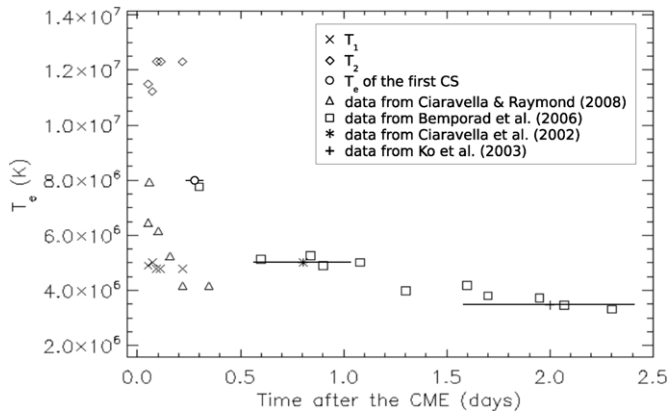


Figure 7. Temporal evolution of the electron temperature in a CS after the ejection of the CME: values from Ciaravella et al. (2002, at $1.5 R_{\odot}$), Ko et al. (2003, at $1.5 R_{\odot}$), Bemporad et al. (2006, at $1.7 R_{\odot}$), and Ciaravella & Raymond (2008, at $1.7 R_{\odot}$) are compared with the T value derived in the present work for the first CS and the T_1 and T_2 values obtained for the second CS.

blueshifts of -0.2 \AA to -0.4 \AA . The intensity ratio of the O VI 1031.9 \AA line to the O VI 1037.6 \AA line is ~ 2 at each heliocentric height of the data set, showing that the O VI lines form only by collisional excitation.

At the heliocentric heights where the CME is detectable only in those lines, no diagnostics is possible. Instead, as we mentioned earlier, at low altitudes ($1.9 R_{\odot}$, at 17:03–17:15 UT and $1.7 R_{\odot}$, at 17:16–17:25 UT) a faint C III 977.0 \AA line shows up. At $1.9 R_{\odot}$ we noticed a peak in C III, at P.A. = 258° – 259° , cospatial with O VI and Ly α peaks, which shows approximately the same Doppler shifts as O VI and Ly α lines ($\sim -0.3 \text{ \AA}$). From the ratio of O VI 1031.9 \AA to C III intensities we inferred an electron temperature $T_e = 2.0 \times 10^5 \text{ K}$, and, from Equation (1), an emission measure $EM = (3 \pm 1) \times 10^{25} \text{ cm}^{-5}$, comparable with that of the second CME.

At $1.7 R_{\odot}$, the C III line shows a single unshifted intensity peak at the same latitude (P.A. = 258° – 260°) of O VI and H I Ly α lines: the electron temperature, $T_e = 1.8 \times 10^5 \text{ K}$, and the emission measure, $EM = 5 \times 10^{25} \text{ cm}^{-5}$, in this feature are of the same order as those previously inferred. We conclude that the physical parameters of the third CME, at least in the few locations where we have been able to infer their values, are of the same order as those derived in the second event.

5.2. Physical Parameters of the CSs

As we have noticed previously, there are no UVCS data to study the CS produced after the third CME, so we can infer the physical parameters only for the CSs that form after the first and the second CMEs, hereafter referred to as the “first” and the “second” CS. Because the Si XII 499.4 \AA and [Fe XVIII] 974.9 \AA lines form only by collisional excitation, in the following we derive the CS electron temperature from Equation (2) and the emission measure from Equation (1), adopting an abundance ratio $\frac{A_{\text{Si}}}{A_{\text{Fe}}} = 1$ (Feldman et al. 1992) and the ionization balances from Mazzotta et al. (1998). As for the length of the CS along the LOS, to facilitate the comparison with values derived by other authors, we used the value proposed by Vrřnak et al. (2009), who assume a typical CS length $L = 10^5 \text{ km}$ at $2.16 R_{\odot}$, with L varying linearly with heliocentric distance. With this assumption, at the height of UVCS observations of the first and the second CME, $L = 8 \times 10^4 \text{ km}$. We point out that any density estimate is strongly affected by the uncertainty in the L parameter, which depends also from the viewing geometry.

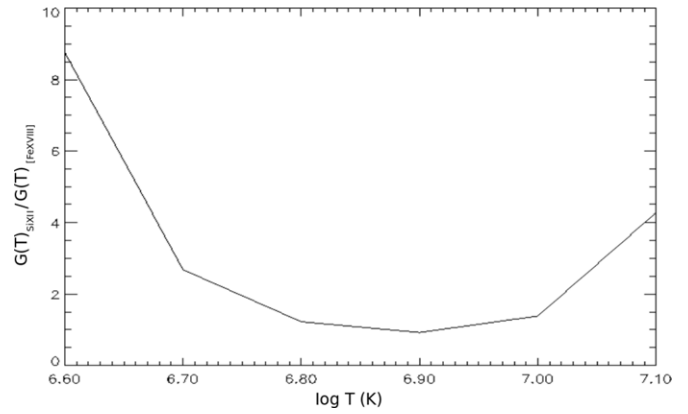


Figure 8. $G(T)_{\text{Si XII}}$ to $G(T)_{[\text{Fe XVIII}]}$ ratio with temperature, using elemental abundances from Feldman et al. (1992) and ionization balances from Mazzotta et al. (1998).

However, Lin et al. (2009) have shown that usually the observed CS thickness does not exceed by more than a factor of 2 its natural thickness, so the projection effects seem not to be, in most cases, very relevant.

5.2.1. The First CS

The CS formed after the 00:30 UT CME has been analyzed using UVCS data taken at $1.7 R_{\odot}$ from 06:08 to 08:18 UT, about 6 hr after the ejection of the first CME. It was detected in UVCS spectra from the [Fe XVIII] line emission ($\log T_{\text{max}} = 6.8$), which shows up only at the P.A. of the white light CS identified in LASCO images. Because it was a faint structure, we summed over the whole time interval and inferred a single value for temperature and density. At this location, the Si XII emission does not show any increase with respect to the quiet Sun emission.

Nevertheless, we have been able to estimate the electron temperature in the CS, assuming an upper limit to the emission of Si XII from the CS of the order of the statistical uncertainty of the Si XII line intensity (10%). From this value and the measured intensity of the [Fe XVIII] line we obtain a value of the electron temperature $T_e = 7.9 \times 10^6 \text{ K}$ and, assuming $EM \simeq N_e^2 L$, an electron density $N_e = 6.0 \times 10^6 \text{ cm}^{-3}$, with an uncertainty of 15%. The temperature estimate is comparable with the values found by other authors (see Figure 7); the value inferred for the electron density is discussed in Section 6.

It looks like the CS temperature might have been underestimated, if the Si XII 499.4 \AA emission is lower than we assumed. However, it turns out that the CS temperature is well identified: this because the profile of the ratio of the contribution functions $\frac{G(T)_{\text{Si XII}}}{G(T)_{[\text{Fe XVIII}]}}$ (where $G(T)_X = A_X C(T)_X$) versus temperature, given in Figure 8, shows that $T_e = 8 \times 10^6 \text{ K}$ corresponds to the minimum of the curve of contribution functions ratio, so that a lower value for the line intensity ratio would not be acceptable.

5.2.2. The Second CS

This CS is detectable in UVCS data at $1.7 R_{\odot}$ over the time interval 09:40–15:58 UT both from [Fe XVIII] and from enhanced Si XII lines emission. We divided the data into five time intervals (09:40–10:10, 10:10–10:40, 10:40–11:10, 11:10–11:55, 11:55–15:58 UT, see images in Figure 5), with the aim of deriving the evolution of electron temperature and density with time.

Table 3
Electron Temperatures and Densities for the Second CS

| Time Interval (UT) | $I(\text{Si XII})/I(\text{Fe XVII})$ | $\log T_1$ | $\log T_2$ | $N_e(T_1)^a$ | $N_e(T_2)^a$ |
|--------------------|--------------------------------------|------------|------------|--------------|--------------|
| 09:40–10:10 | 3 ± 2 | 6.69 | 7.06 | 0.9 | 1.9 |
| 10:10–10:40 | 2.9 ± 1.5 | 6.70 | 7.05 | 1.1 | 2.2 |
| 10:40–11:10 | 4 ± 2 | 6.68 | 7.09 | 1.1 | 3.3 |
| 11:10–11:15 | 4 ± 2 | 6.68 | 7.09 | 1.1 | 3.2 |
| 11:15–15:58 | 4 ± 2 | 6.68 | 7.09 | 1.1 | 3.2 |

Note.

^a In units 10^7 cm^{-3} .

The intensity ratio of Si XII to [Fe XVIII] line and the corresponding electron temperature derived, as explained previously, for each time interval are given in Table 3. For the second CS the $G(T)$ ratios fall in the 2–4 interval. Hence, we found an ambiguity in the estimate of electron temperature, as can be seen from Figure 8, because a unique value of the ratio corresponds to two possible temperature values. This ambiguity might be removed, provided we had observed in the CS a line emitted by a different ion, which, unfortunately, is not the case. Table 3 also gives the electron densities derived from the two values of electron temperature. Both are higher than the values derived for the first CS.

6. DISCUSSION AND CONCLUSIONS

We summarize the results of our work as follows.

1. The three CMEs we analyzed turned out to share some properties. A common characteristic of all events is their low electron temperature. The front of the first two events is at $T_e = 1.6 \times 10^5 \text{ K}$; the temperature estimates we made in the third event yield $T_e = (1.8\text{--}2) \times 10^5 \text{ K}$, although we cannot identify the component of the CME we sampled. It is not unusual to detect CMEs leading edges by enhanced emission in cool lines (see, e.g., Ciaravella et al. 1997, 1999, 2003).
2. Densities in the three events are consistent with estimates made by different authors (see Section 1): assuming an extension along the LOS of the order of $0.5 R_\odot$, or slightly larger, we get, from $\text{EM} \sim 10^{25} \text{ cm}^{-5}$, $N_e \sim 10^7 \text{ cm}^{-3}$. However, it is interesting to note that the second event has a larger density (by a factor of ~ 3) than the previous CME, if LOS is the same. Likely the second CME, slightly southward of the first, implied the opening of a different part of the magnetic system described in Section 4.1, while the third event originated from the same part of the loop system. This hypothesis is also supported by the somewhat different composition of the plasma in the three CMEs, as the first event did not contain any C III, contrary to observations in the other two events.

In conclusion, we propose a scenario where the three ejections originated from magnetic energy release episodes that involved different sections of the magnetic system embedding AR10365. The field disruption in the two earlier CMEs is more catastrophic than in the last event, because the events extend over a larger area (the LASCO CME catalog lists them as “partial halo”), implying interaction with other magnetic systems and because of the acceleration of the CMEs, which progressively decreases from the first to the third event.

The width of the CMEs, as given by LASCO catalog, is $160^\circ\text{--}170^\circ$ in the first two events, and decreases to only 22° in the last event. Vršnak et al. (2007) found a correlation between the CME

width and the acceleration, faster accelerated CMEs tending to be wider. This relationship is only coarsely confirmed here, in that the third event (which has a negative acceleration) is by far the narrowest. Should a higher acceleration be indicative of a higher reconnection rate (see the discussion in Maričić et al. 2007), the present events show that the reconnection rate may affect the CME kinematics, but does not affect the physical parameters of the ejected plasma.

We discuss now the CSs associated with the CMEs, whose position, as previously pointed out, shifts by a few degrees in different events. This change in position is not unexpected, if the scenario previously outlined is correct, and implies that the instabilities, which lead to a breaking in the magnetic configuration and to the formation of the CS, occur, at different times, in different positions within the magnetic system. After every episode, no trace is left of the previous CS, suggesting a reconfiguration of the field that involves also adjacent structures.

Our data set is nearly unique among other CME observations because it covers the initial phase of a CS formation, allowing us to study the CS evolution over a time interval of about 6 hr after its initial formation. As of today, only Ciaravella & Raymond (2008) have studied the evolution of a CS, using UVCS data, from the beginning of the CS formation, while in previous works the properties of the CS have been inferred only at later times, because observations did not include the time of the CS first appearance.

Figure 7 gives the evolution of the electron temperatures of the CS in time, after the CME ejection, as inferred in the present work and in analyses by other authors. Unfortunately, the figure shows that a comparison of the electron temperature of the second CS with previous estimates does not help us solve the ambiguity (see Section 5.2.2) in the selection of the most likely temperature value. However, it turns out that all data collected so far show a slow decrease in time of the CS electron temperature. In individual events where the CS is not destroyed by the occurrence of a later event, the CS cooling may continue over more than 2 days and it is possibly faster over the initial 10 hr. Further data are needed to extend this result to later times and to unambiguously identify the CS behavior in its earliest stage.

One of the open questions about the physics of CSs is what causes their high observed electron temperatures. As in Bemporad et al. (2006) we can check whether the heating can be ascribed to adiabatic compression of the plasma flowing toward the CS. In this case, we can write the relation:

$$\frac{T_{\text{CS}}}{T_0} = \left(\frac{N_{e,\text{CS}}}{N_{e,0}} \right)^{\gamma-1}, \quad (3)$$

where T_{CS} and T_0 are, respectively, the temperatures of the CS and of the quiet corona, $N_{e,\text{CS}}$ and $N_{e,0}$ their electron densities and $\gamma = \frac{c_p}{c_v}$, the ratio of the specific heats at constant pressure and volume ($\gamma = 5/3$ for a monoatomic gas). Using the values of temperatures and densities inferred for the second CS, we show in Figure 9 the evolution in time of the two members of Equation (3).

As expected, over the time interval after the CME ejection (about 5 hr) there is a large discrepancy between the two ratios, so we can conclude that the adiabatic compression is not sufficient to explain the heating of the CS. This result is consistent with Bemporad et al. (2006), who found that only after 2 days from the CME ejection the adiabatic compression becomes a relevant process for the CS heating.

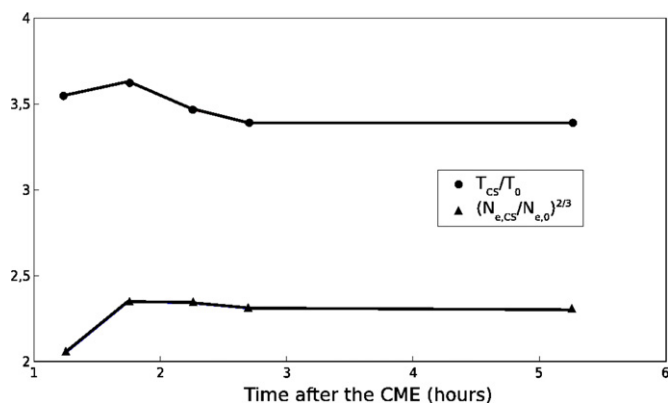


Figure 9. Evolution in time of the two members of the relation 3.

Bemporad (2008) has shown that the kinetic temperature of a CSs, from different events, decreases in time by a factor of ~ 3 over a time interval of about 55 hr after the CME ejection. Kinetic temperatures have been derived from the [Fe XVIII] 974.9 Å line width. Here we analogously inferred the kinetic temperature T_k of the second CS, from the relation:

$$\Delta\lambda = 2\sqrt{\ln 2} \frac{\lambda}{c} \sqrt{\frac{2k_B T_k}{m}}, \quad (4)$$

where $\Delta\lambda$ is the full width at half-maximum (FWHM), λ is the wavelength, k_B is the Boltzmann constant, and m is the ion mass. The FWHM of the [Fe XVIII] line at different times of observation has been computed using a Gaussian fit to the line profile and has been corrected for the instrument profile width (0.32 Å). The comparison between the evolution of T_k with time in the second CS and the estimates from other events is shown in Figure 10, adapted from Bemporad (2008).

The values obtained for the kinetic temperature in the second CS is, in the initial stage of the CS evolution, about a factor of 8 higher than its electron temperature, leading us to conclude that the CS plasma is highly turbulent. It is interesting to note that the profile of the kinetic temperature versus time, at a given altitude, seems independent of individual events, and after ~ 2.3 days, is still about a factor of 2 higher than the electron temperature.

At the time of the CS formation our data give kinetic temperatures of about 4×10^7 K, which decrease by a factor of 2 over 4–5 hr. Ciaravella & Raymond (2008) earliest estimate of T_k referred to this time: earlier data points are not given as the authors tend to ascribe the high values of T_k ($\geq 3 \times 10^7$ K) either to plasmoids traveling along the CS or to the high background caused by the flare. Whatever causes high T_k values at the earliest stages of the CS formation, our data confirm the Ciaravella & Raymond (2008) results. If ascribed to the presence of turbulent motions, the turbulent velocity v_{turb}

$$v_{\text{turb}} = \sqrt{\frac{2k_B}{m_{Fe}} (T_k - T_e)}, \quad (5)$$

would be on the order of 100 km s^{-1} and the turbulent energy density would represent about 3% of the thermal energy density of the CS. The gradual fading of the CS would be related to a progressive decrease of the turbulent energy density, that drops by about a factor of 5 with respect to the thermal energy density 2 days after the CME ejection.

Opposite to the behavior of the electron and kinetic temperatures, that seem not to change in individual CSs, CS densities appear more variable. For instance, Ciaravella & Raymond

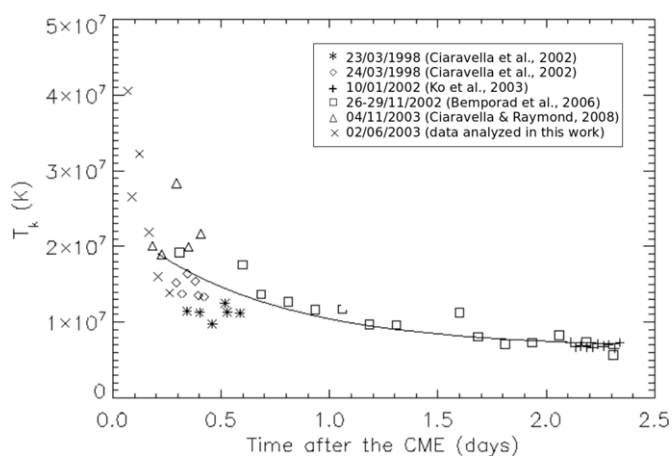


Figure 10. Evolution of kinetic temperature in the CS, as derived from [Fe XVIII] line width, with the time after the CME ejection (adapted from Bemporad 2008). We report the estimates derived by Bemporad (2008) for some events and that from our data (\times).

(2008) densities are higher than present estimates by a factor of 4–10. We may hypothesize that the density (and the magnetic field) of the ambient corona have a role in determining the density within the CS, low densities possibly being related to a low density ambient, evacuated by previous events. This may be the case for the first CME we analyzed: we know that on June 1 at 15:54 UT a CME was ejected from P.A. = 265° , the same angle given for the 00:30 UT CME. Possibly the CS is so tenuous that it is below our detectability threshold (see the delayed appearance of the CS in the first event), until the ambient is adequately replenished. However, density values are affected by the uncertainty in the estimate of the LOS depth of the CS, assumed above to be the same in all events. Until stereoscopic CS observations provide the three-dimensional CS configuration we are unable to reach definitive conclusions about the temporal evolution of CS densities in different events.

The authors acknowledge support from ASI/INAF I/015/07/0. SOHO is a project of international collaboration between ESA and NASA.

REFERENCES

- Bemporad, A. 2008, *ApJ*, **689**, 572
 Bemporad, A., Poletto, G., Suess, S. T., Ko, Y.-K., Schwadron, N. A., Elliott, H. A., & Raymond, J. C. 2006, *ApJ*, **638**, 1110
 Bemporad, A., Raymond, J. C., Poletto, G., & Romoli, M. 2007, *ApJ*, **655**, 576
 Chen, J., Howard, R. A., Brueckner, G. E., Santoro, R., Krall, J., Paswaters, S. E., St. Cyr, O. C., Schwenn, R., Lamy, P., & Simnett, G. M. 1997, *ApJ*, **490**, L191
 Ciaravella, A., & Raymond, J. C. 2008, *ApJ*, **686**, 1372
 Ciaravella, A., Raymond, J. C., & Kahler, S. W. 2006, *ApJ*, **652**, 774
 Ciaravella, A., Raymond, J. C., Kahler, S. W., Vourlidis, A., & Li, J. 2005, *ApJ*, **621**, 1121
 Ciaravella, A., Raymond, J. C., Li, J., Reiser, P., Gardner, L. D., Ko, Y.-K., & Fineschi, S. 2002, *ApJ*, **575**, 1116
 Ciaravella, A., Raymond, J. C., van Ballegooijen, A., Strachan, L., Vourlidis, A., Li, J., Chen, J., & Panasyuk, A. 2003, *ApJ*, **597**, 1118
 Ciaravella, A., et al. 1997, *ApJ*, **491**, L59
 Ciaravella, A., et al. 1999, *ApJ*, **510**, 1053
 Cliver, E. W., Webb, D. F., & Howard, R. A. 1999, *Sol. Phys.*, **187**, 89
 Corti, G., Poletto, G., Suess, S. T., Moore, R. L., & Sterling, A. C. 2007, *ApJ*, **659**, 1702
 Feldman, U., Mandelbaum, P., Seely, J. F., Doschek, G. A., & Gursky, H. 1992, *ApJS*, **81**, 387
 Hori, K., Ichimoto, K., Sakurai, T., Sano, I., & Nishino, Y. 2005, *ApJ*, **618**, 1001

- Hundhausen, A. J. 1987, in Proc. 6th Int. Solar Wind Conf. Vol. 2, The Origin and Propagation of Coronal Mass Ejections, ed. V. J. Pizzo, T. Holzer, & D. G. Sime (NCAR Publ. TN-306; Boulder, CO: NCAR), 181
- Hyder, C. L., & Lites, B. W. 1970, *Sol. Phys.*, **14**, 147
- Ko, K.-Y., Raymond, J. C., Lin, J., Lawrence, G., Li, J., & Fludra, A. 2003, *ApJ*, **594**, 1068
- Lin, J., & Forbes, T. G. 2000, *J. Geophys. Res.*, **105**, 2375
- Lin, J., Ko, Y.-K., Sui, L., Stenborg, G. A., Jiang, Y., Zhao, S., & Mancuso, S. 2005, *ApJ*, **622**, 1251
- Lin, J., Li, J., Ko, Y.-K., & Raymond, J. C. 2009, *ApJ*, **693**, 1666
- Liu, Y., Luhmann, J. G., Lin, R. P., Bale, S. D., Vourlidas, A., & Petrie, G. J. D. 2009a, *ApJ*, **698**, L51
- Liu, Y., Luhmann, J. G., Bale, S. D., & Lin, R. P. 2009b, *ApJ*, **691**, L151
- Mancuso, S., Raymond, J. C., Kohl, J., Ko, Y.-K., Uzzo, M., & Wu, R. 2002, *A&A*, **383**, 267
- Maričić, D., Vršnak, B., Stanger, A. L., Veronig, A. M., Temmer, M., & Roša, D. 2007, *Sol. Phys.*, **241**, 99
- Mazzotta, P., Mazzitelli, G., Colafrancesco, S., & Vittorio, N. 1998, *A&AS*, **133**, 403
- Nelson, G. J., & Melrose, D. B. 1985, in Solar Radiophysics, ed. D. J. McLean & N. R. Labrum (Cambridge: Cambridge Univ. Press)
- Noci, G., Kohl, J. L., & Withbroe, G. L. 1987, *ApJ*, **315**, 706
- Raouafi, N.-E., Mancuso, S., Solanki, S. K., Inhester, B., Mierla, M., Stenborg, G., Delaboudinière, J. B., & Benna, C. 2004, *A&A*, **424**, 1039
- Raymond, J. C., Ciaravella, A., Dobrzycka, D., Strachan, L., Ko, Y.-K., Uzzo, M., & Raouafi, N.-E. 2003, *ApJ*, **597**, 1106
- Raymond, J. C., & Ciaravella, A. 2004, *ApJ*, **606**, L159
- Raymond, J. C., et al. 2000, *Geophys. Res. Lett.*, **27**, 1439
- Schettino, G., Poletto, G., & Romoli, M. 2009, *ApJ*, **697**, L72
- Vršnak, B., & Cliver, E. W. 2008, *Sol. Phys.*, **253**, 215
- Vršnak, B., Maričić, D., Stanger, A. L., Veronig, A. M., Temmer, M., & Roša, D. 2007, *Sol. Phys.*, **241**, 85
- Vršnak, B., et al. 2009, *A&A*, **499**, 905
- Wild, J. P. 1950, *Aust. J. Sci. Res.*, **A3**, 541